Ore Geology Reviews 71 (2015) 203–214

Contents lists available at ScienceDirect

Ore Geology Reviews

journal homepage: www.elsevier.com/locate/oregeorev

The geological significance of Pb–Bi- and Pb–Sb-sulphosalts in the Damajianshan tungsten polymetallic deposit, Yunnan Province, China

Lei Zhang [a,b], Hanjie Wen [a,*], Chaojian Qin [a], Shengjiang Du [a,b], Chuanwei Zhu [a,b], Haifeng Fan [a], Jinrang Zhang [c]

[a] State Key Laboratory of Ore Deposit Geochemistry, Institute of Geochemistry, Chinese Academy of Sciences, Guiyang 550002, China
[b] University of Chinese Academy of Sciences, Beijing 100049, China
[c] Chengdu Institute of Geology and Mineral Resources, China Geological Survey, Chengdu 610081, China

ARTICLE INFO

Article history:
Received 15 August 2014
Received in revised form 18 May 2015
Accepted 20 May 2015
Available online 22 May 2015

Keywords:
Pb–Bi–Sb minerals
Ikunolite
Izoklakeite
Physicochemical conditions
Tungsten polymetallic deposit
Sanjiang

ABSTRACT

The Sanjiang Tethyan domain in SE Asia is one of the most important mineral belts in China. Cu, Pb–Zn, Ag, Au and Sn are the most important resources in this domain, while the tungsten mineralization is poorly reported. In this study, we report on mineralogy in recent discovered Damajianshan (DMJS) tungsten (–Cu–As–Mo–Bi) polymetallic deposit in the southern part of Sanjiang Tethyan domain related to Triassic quartz porphyry. Studies have shown that besides common ore minerals, such as native bismuth, bismuthinite, ikunolite, some specific minerals of Pb–Bi- and Pb–Sb-sulphosalts (e.g. izoklakeite, bournonite, cosalite, and boulangerite) have also been found. Based on paragenetic mineral assemblages, fluid inclusions, and thermodynamic studies, the physicochemical conditions were evaluated for the entire metallogenic process. The sulfur fugacity ($\log f_{S2}$) ranges from −9.7 to −37 with ore-forming temperatures between 190 °C and 330 °C, and the oxygen fugacity ($\log f_{O2}$) ranges from −37.5 to −38.5 when the temperature is 250 °C. The sulfur fugacity and oxygen fugacity show strong fluctuations with broadly negative correlation, indicating that these variations in physicochemical conditions should be responsible for mineral assemblages, and are one of the most significant factors leading to the formation of the DMJS deposit. Our mineralogical studies provide new information for tungsten mineralization and further exploration of tungsten resources in the Sanjiang Tethyan mineralization domain.

1. Introduction

The Sanjiang Tethyan domain in SE Asia is one of the most important mineral belts in China. Numerous studies have shown that the Sanjiang Tethyan domain has experienced a transition of Tethys tectonic evolution in Late Paleozoic to continental collision orogeny in Cenozoic, with multi-stage mineralization and the formation of large volumes of metallic mineral deposits (Liu et al., 1993; Pan et al., 2004; Wang et al., 2010a, 2010b; Deng et al., 2011, 2012). Cu, Pb–Zn, Ag, Au and Sn are the most important resources in this domain (Wang et al., 2014), and the types of deposits present include porphyry-type Cu–Au and Cu–Mo deposits, VMS Cu–Pb–Zn deposits, magmatic-hydrothermal Cu–Ag–Pb–Zn deposits, shear zone-type Au deposits, skarn-type Cu–Mo–Pb–Zn deposits, sedimentary-hosted Pb–Zn–Ag deposits, and others (Deng et al., 2012; Hou et al., 2003, 2007b). In contrast, the tungsten mineralization is poorly understood in the Sanjiang Tethyan domain. Up to date, only some small-scale tungsten ore deposits have been found in the central and northern Sanjiang Region, like Lushui, Shangli-La, Jiangda and Yulong (Deng et al., 2012, 2014a; Hou et al., 2003, 2007b; Hu et al., 2004; Sun et al., 2009; Xue et al., 2007; Zaw, 1990).

Recently, the discovery of the DMJS deposit gave an important impetus for exploration of tungsten resources in this region. The DMJS deposit contains about 0.09 Mt of W, 0.42 Mt of Cu and 0. Mt of As in metal reserves. Preliminary studies have shown that this deposit has abundant Pb–Bi- and Pb–Sb-sulphosalts, besides scheelite, wolframite, chalcopyrite, arsenopyrite, galena, sphalerite and molybdenite. In this study, detailed mineralogical studies have been carried out to identify paragenetic mineral assemblages and their relationship using EPMA analysis. Combining with the fluid inclusions and sulfur isotope ($\delta^{34}S$) systematics, the physicochemical conditions of minerals formation are discussed. The results indicate that the strong fluctuations in physicochemical conditions may have been responsible for the formation of the observed mineral assemblages, and were one of the most significant factors leading to the formation of the DMJS deposit.

2. Geological setting

2.1. Deposit geology

The DMJS deposit is located in Lvchun County, Yunnan Province, China. Tectonically, this deposit is in the southernmost part of the

* Corresponding author.
E-mail address: wenhanjie@vip.gyig.ac.cn (H. Wen).

http://dx.doi.org/10.1016/j.oregeorev.2015.05.017
0169-1368/

Jiangda–Weixi–Lvchun arc-volcanic belt, which was formed at the end of the late Paleozoic to early Mesozoic (Deng et al., 2010, 2012; Hou et al., 2007a, 2007b; Li et al., 1999; Pan et al., 1997; Sone and Metcalfe, 2008; Wang et al., 2013; Yin et al., 2006; Zi et al., 2013) (Fig. 1a, b). The DMJS deposit was first discovered by a 1:200,000 scale regional geological survey by the geological survey of Yunnan Province in the 1970's, and identified as a Cu–As deposit. In recent years, further exploration discovered that it was actually a quartz-vein type tungsten polymetallic deposit related to Triassic quartz porphyry (Fig. 3a).

The DMJS deposit has 0.09 Mt reserves of W metal with an average grade of 0.35 wt.% WO_3 (range 0.15 to 1.2 wt.%) which makes it a large scale W deposit (≥0.05 Mt) according to the industrial classification of ore deposits in China. Subsequent detailed exploration showed that the metal reserves of Cu and As are 0.42 Mt and 0.12 Mt, respectively with ore grades ranging from 0.37 to 3.18 wt.% for Cu and from 2.73 to 27.70 wt.% for As, which means the deposit is classified as intermediate scale for Cu (0.1–0.5 Mt) and large scale for As (≥0.05 Mt). Besides W, Cu, and As, the deposit also contains Pb, Zn, Bi, and Mo in concentrations high enough to be of economic interest.

To date, 10 W-bearing ore bodies have been discovered (Fig. 1d). The ore bodies extend for about 60–430 m vertically and are 3.5–18 m thick (Fig. 1d). Magmatic activity in the deposit is evident by the presence of a Triassic quartz porphyry intrusion and a few lamprophyres. Spatially and temporally, the intrusion of the Triassic quartz porphyry is closely connected to the formation of the DMJS deposit. The W-bearing ore bodies are mainly in the external contact zone of the quartz porphyry, the wall rock being Silurian slates (Fig. 1c, d). Many different types of metasomatic alteration can be found in this deposit, including potassic alteration, silication, sericitization, pyritization, epidotization, and tourmalinization. Faults are the dominant structural features in the study area and they provided favorable metallogenic and ore-hosting space for the movement of ore-forming fluids and the deposition of hydrothermal minerals.

2.2. Ore-forming temperatures

For this fluid inclusion study, representative samples of quartz were collected from several locations in the DMJS deposit. The quartz vein is massive, gray in color and the quartz is always intergrown with sulfide minerals and tungsten ore. The main type of fluid inclusion present is liquid-dominated liquid–vapor inclusions identified based on microscope studies. The inclusions are round or oblong in shape and range in size from 2 to 20 μm but are most commonly in the 5–10 μm range. The vapor phase generally account for 3–5% of the inclusion volume. Raman spectrometry of the gas in the inclusions shows that the main constituents are CH_4 and N_2 with minor amounts of CO_2.

Homogenization temperatures were measured using a THGSM600 type freezing/heating stage calibrated between −196 °C and 600 °C. The homogenization temperatures at the deepest level in the mine (the 512 level, Fig. 1d) were about 290–330 °C, whereas fluid-inclusions temperatures at the highest level (the 889 level, Fig. 1d)

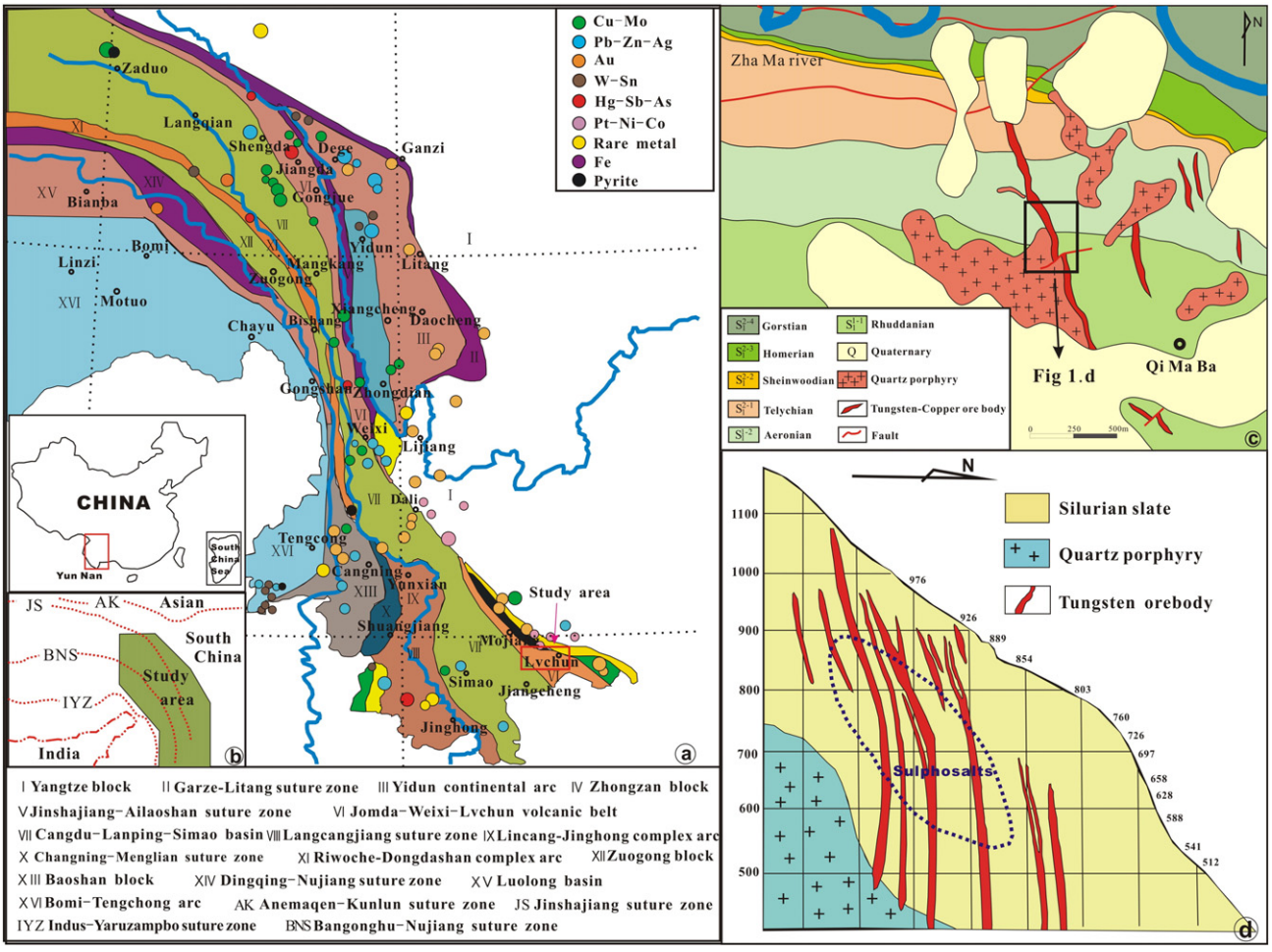

Fig. 1. Geological map of the study area. (a,b)—Geological map showing tectonic framework and distribution of ore deposits in the Sanjiang Tethys (modified after Deng et al., 2010, 2011, 2014b; Hou et al., 2007a, 2007b; Liu et al., 1993); (c,d)—Regional geological and profile map of the Damajianshan tungsten polymetallic deposit, Yunnan.

were 190–220 °C. Apparently, the temperature of the ore-forming fluid decreased gradually as it migrated upwards.

2.3. Mineral assemblage and paragenetic sequence

The ore is characterized by poikilitic, metasomatic and cataclastic textures (Fig. 3b). The deposit includes two main ore types, massive ores and vein ores. The massive ores are a medium grained arsenopyrite–chalcopyrite ores usually with small amounts of pyrrhotite and pyrite. Galena, sphalerite, and several sulphosalts occur in minor amounts. The vein ores are scheelite and wolframite usually with small amounts of molybdenite and manganocalcite (Fig. 3a, b, f). The mineral assemblage is arsenopyrite, pyrite, chalcopyrite, galena, sphalerite, pyrrhotite and Pb–Sb–Bi series minerals (Fig. 3b), and the elements are associated with As, Fe, Cu, Pb, Zn, Sb, Bi and S. The metal sulfides are always present as idiomorphic, hypidiomorphic and allotriomorphic granular masses. Poikilitic-dissolutive, inclusive, and wrapped textures are very common in the metal sulfides. Based on the cross-cutting and inclusion relationships, chalcopyrite, pyrite, galena, and native bismuth formed significantly later than arsenopyrite (Fig. 3b). The native bismuth always occurs intimately with galena or as veinlets at the grain boundaries of sulfides. Genetically, native bismuth and galena are closely related (Fig. 6).

The ore mineralogy in DMJS deposit is complex. The main ore minerals are arsenopyrite, pyrite, chalcopyrite, scheelite, wolframite, galena, sphalerite, molybdenite, pyrrhotite, bournonite, cassiterite, boulangerite and several bismuth minerals (including native bismuth, bismuthinite, cosalite, izoklakeite and ikunolite). The gangue minerals are quartz, dolomite, manganocalcite, sericite, chlorite and others. It is very common for these minerals to occur as mutual metasomatic inclusions and interpenetrations. According to the mineral intercalating relationships, the mineral formation sequence had four stages (Figs. 2, 3). From the earliest to latest, the four stages can be classified as silicate, quartz–sulfide, sulfide–oxide and carbonate. The Bi–Sb minerals were formed during the two middle stages, the sulfide stages. The paragenetic sequence of the DMJS deposit is shown in Fig. 2. The observations that were used to define these four sequential stages are as follows:

The silicate stage is characterized by quartz veins with clean contacts. These veins contain few or no sulfides. These quartz veins are always cut by ore-bearing veins which are formed in the later stages (Fig. 3c).

The quartz–sulfide stage is characterized by the widespread occurrence of chalcopyrite and arsenopyrite, with minor pyrite, sphalerite, galena and pyrrhotite. These ore minerals are always cut the early quartz veins (Fig. 3c).

The sulfide–oxide stage consists mainly of sulfides and W-bearing minerals (Fig. 3d), with minor molybdenite, native bismuth, bismuthinite, bournonite, and the Pb–Bi- plus Pb–Sb-sulphosalt minerals. The Bi–Sb-bearing minerals, especially the Pb–Bi- and Pb–Sb-sulphosalts, were formed late in the sulfide–oxide stage. Native bismuth, Pb–Bi- and Pb–Sb-sulphosalt minerals are always present along the boundaries or in the fissures of galena grains (Fig. 3e).

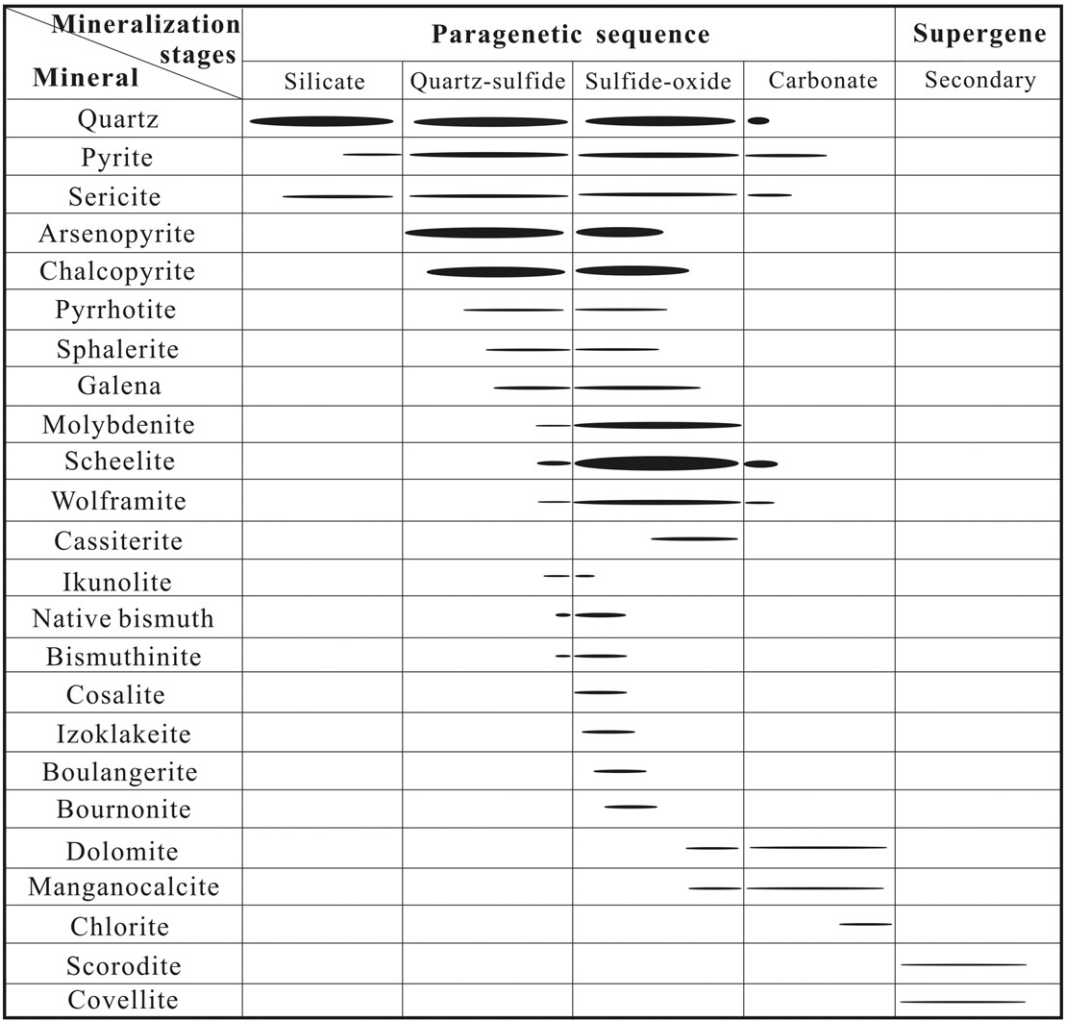

Fig. 2. Paragenetic sequence of minerals in the DMJS deposit.

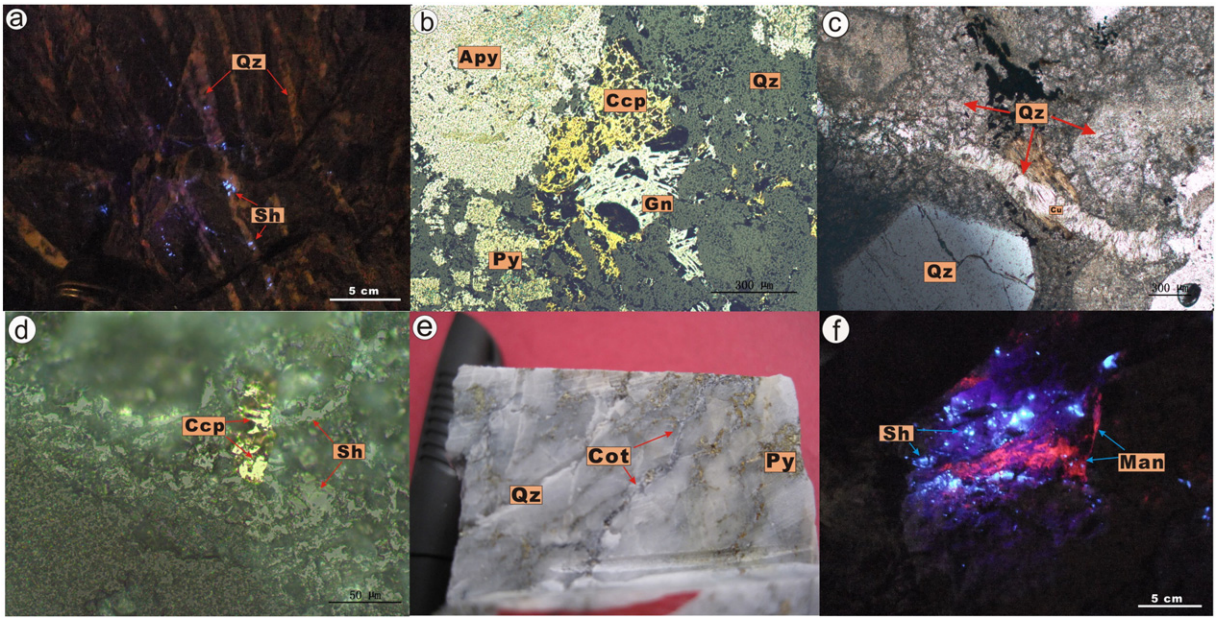

Fig. 3. Photographs and photomicrographs about deposit type and minerals assemblages of the DMJS deposit. (a) Scheelite diseases in quartz veins or attach to the quartz vein walls. (b) Arsenopyrite intergrowths with chalcopyrite, pyrite and galena, and its formation earlier than other sulfides (reflected light). (c) Later Cu-bearing quartz vein cutting the early non-mineralized quartz vein (plane-polarized light). (d) Scheelite intergrowths with chalcopyrite (reflected light). (e) Cosalite ore vein in the quartz. (f) Disseminated scheelite in quartz and closely associated with manganocalcite under fluorescent light. Qz—quartz; Sh—scheelite; Py—pyrite; Gn—galena; Apy—arsenopyrite; Ccp—chalcopyrite; Cot—cosalite; Man—manganankerite.

The later carbonate stage is marked by the appearance of carbonate. The calcite and dolomite veins contain almost no sulfides or tungsten minerals. They always cut the early quartz–sulfide veins (Fig. 3f).

3. Samples and analytical methods

There are 13 levels at the DMJS deposit, which range in elevation from 512 m above mean sea level to 976 m (Fig. 1d). Some of the levels

Table 1
Chemical compositions of bismuth sulfide minerals by EPMA analysis (%).

Number	S	Fe	As	Cu	Pb	Zn	Sb	Bi	Mo	Total	Calculated formula
Native bismuth (Bi)											
512-4-9	0.02	0.22	–	0.37	–	–	0.09	95.77	–	97.03	$Bi_{0.97}$
512-7-8	–	–	–	0.05	–	0.04	0.03	97.28	–	97.65	$Bi_{0.98}$
976-11-3	0.03	0.52	–	–	–	–	0.02	96.64	–	97.56	$Bi_{0.98}$
976-11-5	–	1.07	–	–	–	–	0.02	98.02	–	99.40	$Bi_{0.99}$
976-11-6	0.07	0.69	–	–	0.11	0.04	0.09	97.18	–	98.50	$Bi_{0.99}$
976-11-8	0.02	0.71	–	–	–	0.05	0.11	96.77	–	98.00	$Bi_{0.98}$
976-11-14	0.02	0.66	–	–	–	0.03	0.06	96.85	–	97.95	$Bi_{0.98}$
Mean	0.03	0.55	–	0.06	0.02	0.02	0.06	96.93	–	98.01	$Bi_{0.98}$
Bismuthinite (Bi_2S_3)											
512-4-8	19.09	0.13	–	0.55	2.08	–	0.67	76.40	0.04	99.41	$Bi_2S_{3.26}$
541-2-12	17.09	0.15	–	0.10	–	–	0.43	79.25	–	98.69	$Bi_2S_{2.81}$
541-2-13	17.34	0.09	–	0.14	–	–	0.08	82.22	0.09	100.94	$Bi_2S_{2.75}$
541-2-18	18.66	0.63	–	0.22	–	–	0.10	79.47	0.10	100.09	$Bi_2S_{3.06}$
541-2-20	19.30	0.13	–	0.11	–	–	0.06	78.91	0.10	99.47	$Bi_2S_{3.19}$
541-2-29	19.12	0.08	–	0.18	–	–	0.32	80.24	0.03	100.79	$Bi_2S_{3.11}$
Mean	18.43	0.20	–	0.22	0.35	–	0.28	79.41	0.06	99.90	$Bi_2S_{3.03}$
Ikunolite (Bi_4S_3)											
541-2-14	10.65	0.11	–	0.09	0.13	–	–	88.27	0.02	99.68	$Bi_4S_{3.14}$
541-2-15	9.11	0.14	–	0.10	0.04	–	–	86.96	0.03	97.15	$Bi_4S_{2.74}$
541-2-21	9.97	0.35	–	0.03	–	–	–	89.52	–	100.34	$Bi_4S_{2.90}$
541-2-25	10.56	0.26	–	–	1.22	–	0.09	86.86	–	99.37	$Bi_4S_{3.16}$
541-2-28	10.64	0.17	–	0.07	–	–	–	87.69	0.04	98.96	$Bi_4S_{3.16}$
Mean	10.19	0.20	–	0.06	0.28	–	0.02	87.86	0.02	99.10	$Bi_4S_{3.02}$
Galena (PbS)											
512-7-5	13.78	0.08	–	0.19	85.36	–	–	0.21	–	99.67	$PbS_{1.04}$
512-8-8	13.50	0.06	–	–	85.16	–	–	0.38	–	99.13	$PbS_{1.02}$
512-8-11	13.61	0.04	–	0.04	85.93	0.02	–	0.55	–	100.21	$PbS_{1.02}$
541-2-7	13.49	0.26	–	0.45	85.89	–	–	–	–	100.20	$PbS_{1.01}$
541-2-11	13.50	0.04	–	–	85.84	–	–	–	–	99.54	$PbS_{1.02}$
889-3-6	13.70	0.25	–	0.47	84.67	–	–	0.39	–	99.49	$PbS_{1.05}$
889-3-3	13.27	0.40	0.08	0.11	84.46	–	–	–	–	99.04	$PbS_{1.02}$
Mean	13.55	0.16	–	0.18	85.33	–	–	0.22	–	99.61	$PbS_{1.03}$

could not be entered because closure due to mining have been completed. The 23 samples were collected from the 512, 541, 588, 726, 803, 889, and 976 levels. The minerals analyzed by EPMA were arsenopyrite, pyrite, chalcopyrite, scheelite, wolframite, galena, sphalerite, molybdenite, pyrrhotite, bournonite, native bismuth, ikunolite, and Pb–Bi- and Pb–Sb-sulphosalts. This manuscript mainly deals with the minerals galena, native bismuth, bismuthinite, ikunolite, and the Pb–Bi- and Pb–Sb-sulphosalts. The nine correlative samples are mainly collected from the 512, 541, 588, 889, and 976 levels. The spatial distribution of these samples is relatively uniform and we believe they represent typical ore. Ore mineral assemblages include scheelite, chalcopyrite, pyrite, pyrrhotite, marmatite and galena, with Bi–Sb minerals as inclusions in the sulfides.

Systematic studies of the speciation and distribution of Bi–Sb minerals were performed at the State Key Laboratory of Ore Geochemistry, Institute of Geochemistry, Chinese Academy of Sciences, Guiyang, China (IG-CAS), using a Shimadzu EPMA-1600 electron microprobe equipped with an energy-dispersive spectrometer (EDS), and back-scattered electron (BSE) imaging capability. BSE analyses were carried out at 1000–4000 times magnification, with an accelerating voltage of 25 kV and beam current of 4.5 nA. Instrument conditions for wavelength-dispersive spectrometer (WDS) analyses were set to 25 kV accelerating voltage, a 20 nA beam current, and a 10 μm electron beam spot diameter, and 10 s count times for unknown or background probe sites. The minimum detection limits for Bi, Sb, Cu, Fe, Pb, Mo, Cr, Zn, As, and S were 0.02%. The selected analytical spectral lines and deducted background values were achieved using instrument programs, and some fault spectral peaks were calibrated artificially in the process of energy spectrum analysis. All related analytical procedures were performed at IG-CAS in Guiyang. All data are stated in terms of weight percent. We selected chemical analyses with totals between 98 and 102% and these mineral analyses are presented in Tables 1 and 2. BSE images of coexisting minerals are shown in Figs. 4–6.

4. Results

4.1. Chemical compositions and textures

EPMA and BSE analytical data showing mineral chemical compositions, textures, and assemblages of Bi-bearing sulfide minerals and sulphosalts in the deposit are presented in Tables 1 and 2 and illustrated in Figs. 4–6. Ore mineral assemblages include arsenopyrite, pyrite, chalcopyrite, scheelite, wolframite, galena, sphalerite, molybdenite, pyrrhotite, native bismuth, bismuthinite, ikunolite, cassiterite, with Pb–Bi- and Pb–Sb-sulphosalts (bournonite, boulangerite, cosalite and izoklakeite) included in the sulfides. Note that ikunolite and izoklakeite which are not common, have been identified in the deposit.

4.1.1. Bi-bearing sulfide minerals

Native bismuth is always closely associated with galena and other Bi-bearing minerals and it usually has a dendritic, veinlet, milk-drop, or irregular granular appearance. It generally occurs as irregular grains ranging in size from 2 to 20 μm, rarely as large as 30 μm in size. The Bi content of native bismuth in the deposit ranges from 97.03 to 99.40 wt.%. The total trace element contain of the native bismuth is 0.60–2.97%. These trace elements can include Au, Ag, Te, and Se (Zhong et al., 2005; Dimitrova and Kerestedjian, 2006; Ye et al., 2014). Bismuthinite was locally enriched in the deposit. It is present as long columnar or acicular crystals, but aggregates had radiant columnar or granular crystals with joint surfaces lacking horizontal stripes

Table 2
Chemical compositions of bismuth–antimony sulphosalt minerals by EPMA analysis (wt.%).

Number	S	Fe	As	Cu	Pb	Zn	Sb	Bi	Mo	Total	Calculated formula
Cosalite ($Pb_2Bi_2S_5$)											
512-4-2	16.74	0.08	–	0.28	40.29	–	0.15	42.45	–	100.46	$Pb_{1.96}Bi_{2.04}S_{5.25}$
512-4-5	16.71	0.08	–	0.29	40.85	–	0.33	41.53	–	99.92	$Pb_{1.99}Bi_{2.01}S_{5.27}$
541-2-2	16.95	0.31	–	0.53	39.59	–	1.28	40.69	–	99.56	$Pb_{1.98}Bi_{2.02}S_{5.48}$
541-2-22	16.97	0.27	–	0.39	40.05	–	1.44	40.92	–	100.39	$Pb_{1.99}Bi_{2.01}S_{5.44}$
541-5-19	15.99	1.01	0.09	0.13	47.72	–	0.31	33.68	–	99.54	$Pb_{2.35}Bi_{1.65}S_{5.09}$
588-29-3	16.83	1.72	0.40	0.37	39.35	–	0.88	39.97	–	99.78	$Pb_{1.99}Bi_{2.01}S_{5.51}$
588-81-1	16.27	0.21	–	0.15	40.80	–	0.91	40.47	–	99.05	$Pb_{2.02}Bi_{1.98}S_{5.19}$
Mean	16.64	0.53	0.07	0.30	41.23	–	0.76	39.96	–	99.82	$Pb_{2.04}Bi_{1.96}S_{5.32}$
Bournonite ($PbCuSbS_3$)											
588-4-14	20.94	0.03	0.70	12.91	42.47	–	22.55	0.06	–	99.67	$Pb_{0.94}Cu_{0.93}Sb_{0.85}S_3$
588-4-15	20.98	–	0.68	12.96	41.77	–	22.51	–	–	98.91	$Pb_{0.92}Cu_{0.93}Sb_{0.85}S_3$
588-4-16	21.14	0.03	0.77	12.96	42.08	–	23.06	0.24	–	100.27	$Pb_{0.92}Cu_{0.93}Sb_{0.86}S_3$
588-4-17	21.20	0.02	0.81	12.70	41.71	–	22.90	–	–	99.35	$Pb_{0.91}Cu_{0.90}Sb_{0.85}S_3$
588-4-18	21.22	0.02	0.68	13.01	41.89	–	21.46	0.07	–	98.34	$Pb_{0.92}Cu_{0.93}Sb_{0.80}S_3$
588-4-19	21.09	–	0.80	12.93	41.73	–	21.74	–	–	98.32	$Pb_{0.92}Cu_{0.93}Sb_{0.81}S_3$
Mean	21.21	0.05	0.74	12.91	41.94	–	22.37	0.06	–	99.14	$Pb_{0.92}Cu_{0.93}Sb_{0.84}S_3$
Izoklakeite ($Pb_{27}(Cu,Fe)_2(Sb,Bi)_{19}S_{57}$)											
588-4-1	18.30	0.04	–	1.18	45.67	–	9.03	23.81	–	98.07	$Pb_{22}(Cu,Fe)_2Sb_7Bi_{11}S_{57}$
588-4-2	18.50	0.05	–	1.25	45.39	–	10.11	21.07	–	96.40	$Pb_{22}(Cu,Fe)_2Sb_8Bi_{10}S_{58}$
588-4-3	18.89	–	0.23	1.21	46.97	–	13.55	15.12	–	96.00	$Pb_{23}(Cu,Fe)_2Sb_{11}Bi_7S_{59}$
588-4-6	19.40	0.06	0.23	1.26	47.71	–	14.89	14.61	–	98.21	$Pb_{23}(Cu,Fe)_2Sb_{12}Bi_7S_{61}$
588-4-8	18.24	0.04	–	1.16	45.14	–	8.97	22.21	–	95.86	$Pb_{22}(Cu,Fe)_2Sb_7Bi_{11}S_{57}$
588-4-23	17.22	0.07	–	1.13	44.64	–	7.63	25.30	–	96.08	$Pb_{22}(Cu,Fe)_2Sb_6Bi_{12}S_{54}$
Mean	18.43	0.22	0.08	1.20	45.92	–	10.70	20.35	–	96.77	$Pb_{22}(Cu,Fe)_2Sb_9Bi_{10}S_{58}$
Boulangerite ($Pb_5Sb_4S_{11}$)											
588-4-12	19.60	0.02	0.59	0.11	53.69	–	20.71	3.22	–	97.94	$Pb_{5.19}(Sb, Bi, As)_{3.87}S_{12.25}$
588-4-13	19.85	0.03	0.61	0.28	55.01	–	21.07	2.16	–	99.04	$Pb_{5.31}(Sb, Bi, As)_{3.83}S_{12.40}$
588-4-20	19.70	0.03	0.39	0.15	53.08	–	21.65	2.81	–	97.83	$Pb_{5.13}(Sb, Bi, As)_{3.93}S_{12.31}$
588-4-21	19.50	–	0.47	0.23	53.69	–	18.86	4.63	–	97.51	$Pb_{5.19}(Sb, Bi, As)_{3.67}S_{12.19}$
588-4-24	19.67	0.03	0.51	0.02	53.89	–	21.41	3.14	–	98.79	$Pb_{5.21}(Sb, Bi, As)_{3.95}S_{12.29}$
588-4-25	19.80	–	0.51	0.04	53.27	0.02	21.32	2.37	–	97.45	$Pb_{5.15}(Sb, Bi, As)_{3.86}S_{12.38}$
588-4-26	19.54	–	0.60	0.12	53.37	–	21.06	3.11	–	97.91	$Pb_{5.16}(Sb, Bi, As)_{3.92}S_{12.21}$
588-4-22	19.82	0.02	0.56	0.11	53.02	–	21.17	3.75	–	98.46	$Pb_{5.12}(Sb, Bi, As)_{4.05}S_{12.39}$
Mean	19.69	0.03	0.53	0.13	53.63	–	20.91	3.15	–	98.12	$Pb_{5.18}(Sb, Bi, As)_{3.88}S_{12.30}$

(Fig. 4c). The ikunolite has a lead-gray distinctly metallic luster. The structure, physical and optical properties of the ikunolite were very similar to bismuthinite but its surfaces are smoother (Fig. 4c). The EPMA analysis totals for ikunolite were between 97.15 and 100.34 wt.%, with an average value of 99.1 wt.%, and EDS analysis indicated that Se and Te were not present in concentrations above their detection limits. Ikunolite is one of the minerals of the tetradymite series and the ikunolite at the DMJS deposit is very close to the end-member composition of Bi_4S_3. Galena is always closely related to bismuth minerals and it is able to incorporate a small amount of bismuth within its structure.

4.1.2. Sulphosalts

There are a number of different Pb–Bi- and Pb–Sb-sulphosalts such as cosalite, bournonite, izoklakeite, and boulangerite in the DMJS deposit. They are useful associated components and widely distributed in the deposit. Because their grains are too small to obtain reliable X-ray diffraction data, we characterized them based on their optical properties, chemical compositions, and coexisting mineral assemblages. Cosalite is common in the deposit; it formed in the late sulfide stage. It occurs in hand specimen as acicular crystals with a metallic luster (Fig. 3e). Bournonite has three different crystal morphologies and habits and occurs as granular polyhedrons or as short prismatic or long columnar crystals. The surfaces of bournonite grains typically have many corrosion pits (Fig. 5d), and it is darker than other Bi–Sb sulfosalt minerals in the BSE images. Compared with the electron probe standard data for bournonite (Jin, 1986), the bournonite in the DMJS deposit has a higher S and lower Sb and Pb contents (Table 2). To date, only the Yaogangxian tungsten deposit in Yichang City, Hunan Province, has produced good quality bournonite crystal (Wang and Niu, 1994). The izoklakeite crystal morphology is long columnar and needle-like crystals (Fig. 5b, c). As their grain sizes are too small leading the EPMA analysis results having deviation, the calculated chemical formula of izoklakeite do not fit its ideal formula well (Table 2). The boulangerite has a lead gray metallic luster, and an irregular granular habit. It looks very similar to galena in the BSE images. and its surface always had solution pores (Fig. 4d). By the same reason, the calculated chemical formula of boulangerite also do not fit its ideal formula well (Table 2). They all show the characteristic of S-rich.

4.2. Relationships between sulphosalts and related minerals

Detailed optical microscopy and EPMA analysis have also permitted investigation of textural relationships and compositional variations between minerals. Cosalite is a rather common sulphosalt species in the DMJS deposit and is always intergrown with pyrite, pyrrhotite, chalcopyrite, arsenopyrite, galena, native bismuth, or bismuthinite (Figs. 3e, 5a, 6). Small amounts of Cu and Fe are commonly present in the cosalite, substituting for Pb (Table 2). Cosalite shows a range of compositions including an Sb-rich varieties (containing up to 1.44 wt.% Sb, respectively). This implies partial Sb substitution into the cosalite structure. Bournonite is opaque and always intergrown with scheelite, arsenopyrite, chalcopyrite, galena, or boulangerite (Fig. 5d. see also Martínez Frías, 1991). It usually fills small voids and fractures as twinned polycrystalline aggregates. Boulangerite, in the form of radial, fibrous crystals, always appears associated with galena and bournonite. It looks very much like galena in BSE images, and its surface always has

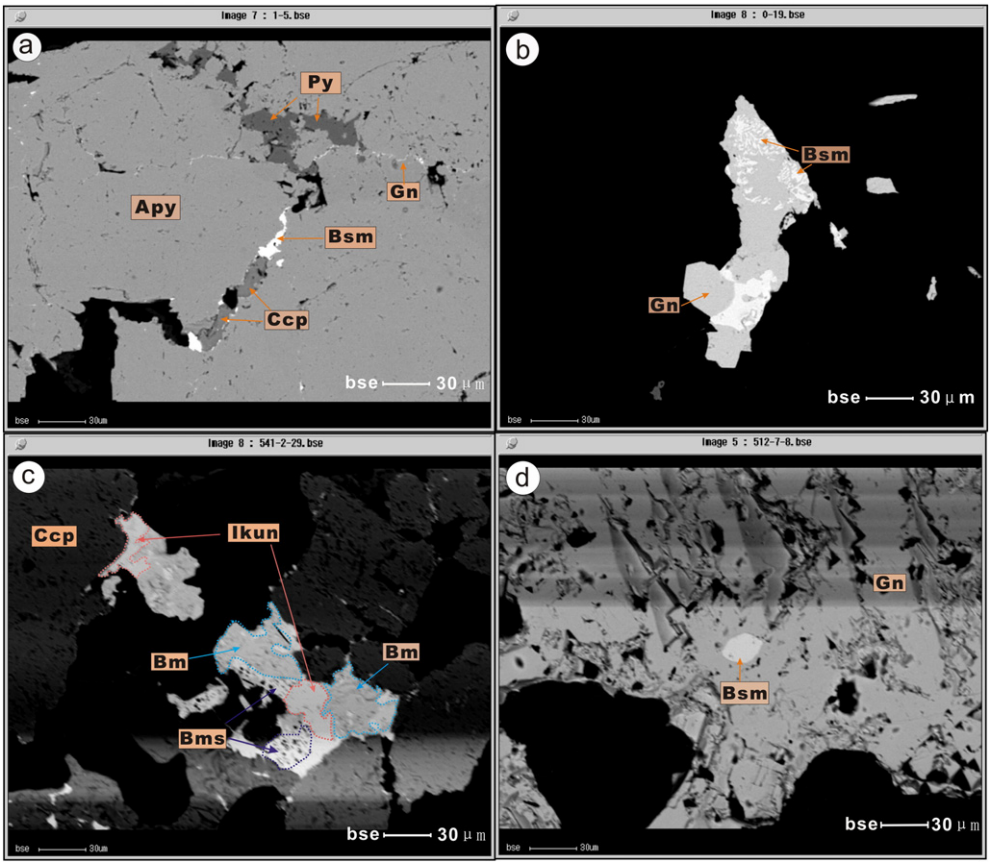

Fig. 4. Back scattered electron images of bismuth sulfide minerals from the DMJS deposit. (a) Galena intergrown with native bismuth, pyrite, chalcopyrite, arsenopyrite as infill veinlets along cracks (interstitial) in arsenopyrite, indicating arsenopyrite is formed the earliest. (b) The vermicular exsolution texture of native bismuth in galena, (c) ikunolite decomposed into bismuthinite and native bismuth during cooling. (d) The milk-drop exsolution texture of native bismuth in galena, indicating native bismuth precipitates from molten state. Py—pyrite; Gn—galena; Apy—arsenopyrite; Bsm—native bismuth; Bm—bismuthinite; Ccp—chalcopyrite; Ikun—ikunolite.

holes (Fig. 5d). The composition of the izoklakeite in the DMJS deposit is similar to that in other mineral deposits but the DMJS izoklakeite is Bi-rich and Pb-poor (Table 3). Izoklakeite intergrowths occur in cosalite, galena, chalcopyrite, arsenopyrite, sphalerite, and native bismuth (Fig. 5b, c). In view of the complex mineralogy encountered in this W deposit, we speculate that additional sulphosalt minerals may be identified.

5. Discussion

5.1. The discovery of the Pb–Bi- and Pb–Sb-sulphosalts

Sulphosalt minerals exist principally in hydrothermal deposits, especially in magmatic hydrothermal deposits. During ore-forming processes, many types of sulphosalt minerals are formed in the late stages of mineralization, always later than oxysalt minerals (scheelite, cassiterite, etc) and the main sulfide ones (arsenopyrite, pyrite, chalcopyrite, etc). Generally, the sulphosalts form in the middle-late part of the quartz–sulfide stage or the early part of the sulfide–oxide stage. The formation of bismuth sulphosalt minerals occurs later than native bismuth and bismuthinite, but earlier than arsenic-antimony sulphosalt minerals. Spatially, the main Bi sulphosalts occur close to the granite, while As–Sb sulphosalts occur far away from it in the magmatic hydrothermal deposit (Luo and Jiang, 1992). In addition, Bi–Sb sulphosalts are carriers of some precious scattered elements (Cook et al., 2011; Xu and Shao, 1982).

Izoklakeite is not common in nature. The izoklakeite in the DMJS deposit is only the second reported occurrence in China. The other occurrence is in massive cassiterite-multi-metal sulfide ores in the Mangchang deposit in Guangxi, China (Wei and Zhang, 1991). Crystallographic studies (Zakrzewski and Makovicky, 1986) showed that the izoklakeite belongs to the kobellite ($Pb_5(Bi, Sb)_8S_{17}$) series (with Bi > Sb), which includes the end members giessenite ($Cu_{4.27}Pb_{51.75}Bi_{32.19}Sb_{7.79}S_{116.18}$) and tintinaite ($Pb_5(Sb, Bi)_8S_{17}$) (with Bi < Sb). Different minerals in this series are distinguished by their Ag, Cu, and Fe content. Our chemical analyses suggest that izoklakeite is a solid solution, with differing degrees of isomorphic replacement; thus, the contents of Pb, Bi, Sb, Ag, and S are within specific ranges but are not fixed values.

Ikunolite is also not common in nature and is only found in a few places worldwide although it does occur in a number of different types of deposits. It has been reported from a sulphosalt-rich vein-type sulfide deposit in Skellefteå, Sweden (Wagner and Jonsson, 2001); an iron deposit in the Martinovo area, Bulgaria (Dimitrova and Kerestedjian, 2006); gold veins in southeast British Columbia, Canada (Cook et al., 2007a, 2007b); and a gold-rare metal deposit in northeast Russia (Zhang, 2000). The ikunolite that Dimitrova and Kerestedjian (2006) found in post-skarn sulfide–arsenide mineralization in the Martinovo deposit was closely associated with native bismuth and bismuthinite. They divided the bismuthinite there into two types (BS1 and BS2) using mineral structure, physical, and optical properties. Because the native bismuth and BS2 always grew together with a vermicular texture, they speculated that they formed because of decomposition of ikunolite during cooling (from the reaction $2Bi_4S_3 + 1.5S_2 = 3Bi_2S_3 + 2Bi$). This texture had previously been described by Ramdohr (1980), Chatterjee and Smith (2000), and Koszowska (2004), but they all interpreted the texture as being the result of exsolution.

Boulangerite and bournonite are always intergrown with each other. The bournonite shows a homogeneous composition, with minor quantities of As. It is important to point out the absence of As in all the grains

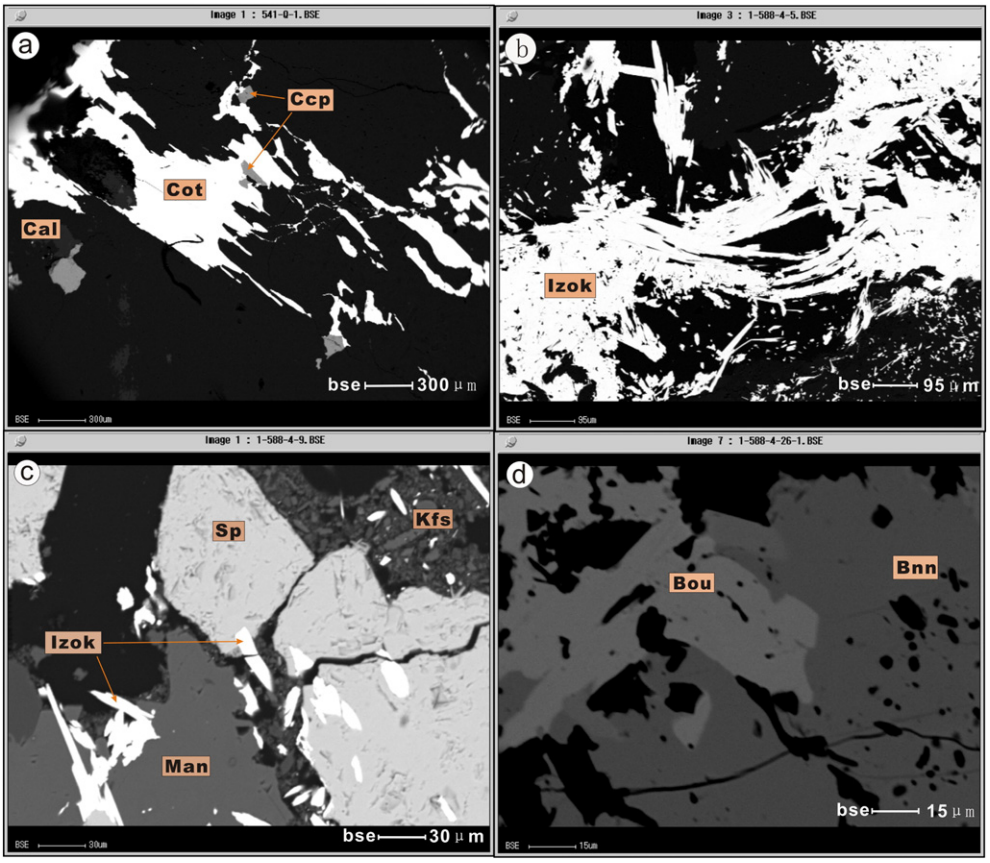

Fig. 5. Back scattered electron images of bismuth–antimony sulfosalt minerals from the DMJS deposit. (a) Needle-like structure of cosalite. (b) Needle clusters of izoklakeite. (c) Izoklakeite replacing sphalerite, manganankerite and K-feldspar. (d) Bournonite intergrowths with the Boulangerite. Cot—cosalite; Cal—calcium carbonate; Izok—izoklakeite; Man—manganankerite; Sp—sphalerite; Kfs—k-feldspar; Bnn—bournonite; Bou—Boulangerite.

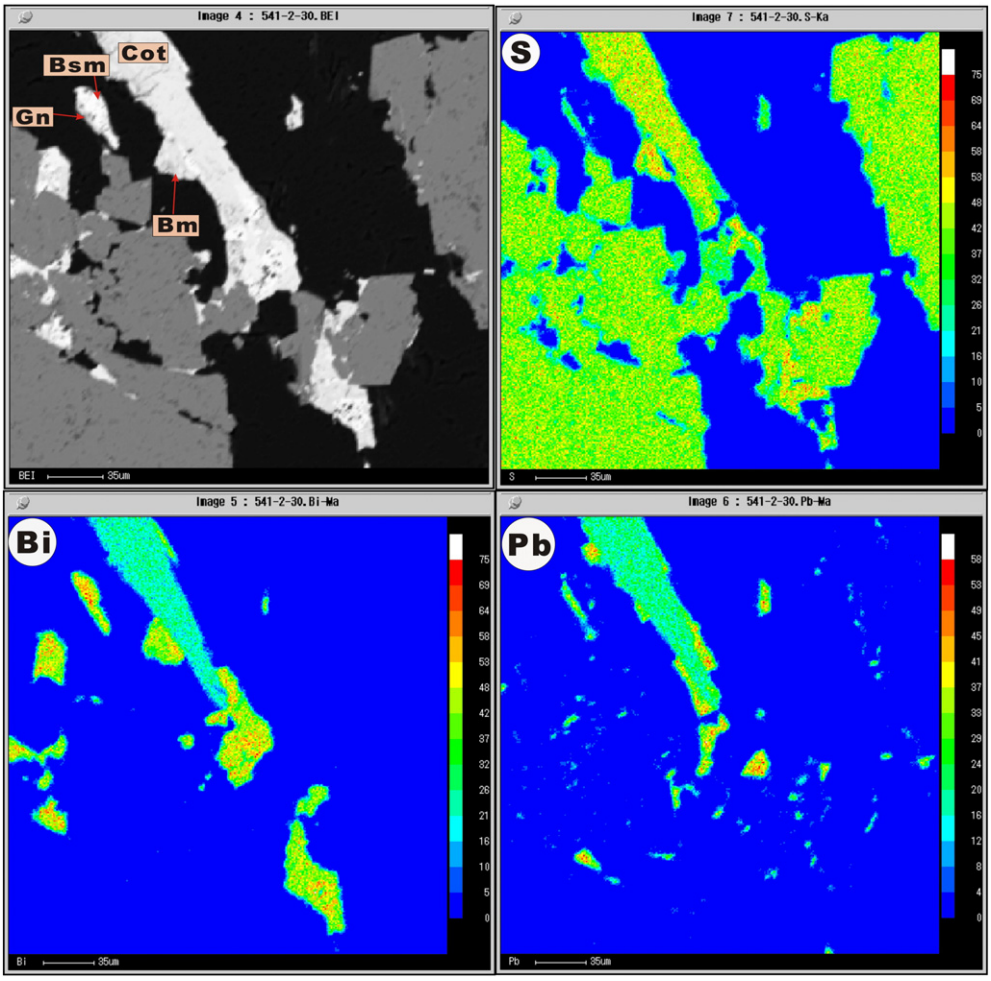

Fig. 6. EPMA element map and BSE images of the mineral paragenesis: cosalite, bismuthinite, galena and native bismuth. Cot—cosalite; Gn—galena; Bsm—native bismuth; Bm—bismuthinite.

analyzed (Table 2). An isomorphic substitution between bournonite and seligmannite ($CuPbAsS_3$) commonly occurs in nature (Martínez Frías, 1991 and Fig. 5d). This substitution could indicate the existence of a chemical splitting during the Sb–As sulphosalts crystallization related to the trend for Bi → Sb → As with decreasing temperature (Kostov and Stefanova, 1981). The compositional homogeneity of the bournonite could indicate the existence of a tendency for the Sb and As sulphosalts to crystallize as separate phases as the fluid temperature gradually decreased (Kostov and Stefanova, 1981). These characteristics are consistent with the sequence in which the Bi–Sb–As-sulphosalts in the DMJS deposit were formed.

5.2. Hydrothermal physicochemical conditions

5.2.1. Temperature and pH

Temperature is one of the most important characteristics of a hydrothermal fluid. As temperature decreases, minerals crystallize and precipitate from the fluid forming different types of deposits. Temperature also affects oxygen and sulfur fugacities which also contribute to mineral precipitation. As oxygen and sulfur fugacities decrease with decreasing temperature, oxidation–reduction processes are weakened and simple substances become more stable (Zhang et al., 2013). Based on our study of the homogenization temperature of fluid inclusions

Table 3
A comparison for chemical compositions (wt.%) of izoklakeite and boulangerite from the DMJS deposit with other izoklakeite and boulangerite records (the data in the table are partial, "—" signifies lower than detection limit or unmeasured data).

S	Pb	Sb	Bi	Cu	Fe	Ag	As	Total	Data Source
Izoklakeite									
18.43	45.92	10.70	20.35	1.20	0.05	—	0.08	96.77	This paper, 2014
17.22	45.37	12.95	20.78	1.10	0.18	1.97	—	99.56	Wei and Zhang (1991)
17.00	46.60	13.30	20.50	1.00	0.20	2.00	—	100.6	Harris and Roberts (1986)
16.91	50.01	11.67	19.20	0.88	0.19	0.59	—	99.45	Zakrzewski and Makovicky (1986)
Boulangerite									
19.69	53.63	20.91	3.15	0.13	0.03	—	0.53	98.12	This paper, 2014
18.77	54.56	25.42	0.4	—	—	—	—	99.31	Wagner et al. (2005)
18.84	54.21	26.61	0.14	—	—	—	0.24	100.05	Ventruti et al. (2012)
17.8	52.9	22.2	—	—	—	—	—	—	Achimovičová and Balaž (2008)
18.63	54.95	26.39	—	—	—	—	—	—	Pruseth et al. (2001)

from the DMJS deposit, we found that the ore-forming temperature was between 190 °C and 330 °C meaning that the deposit was formed from a medium-high temperature hydrothermal system. Samples collected from the 512 level in the DMJS deposit had equilibration temperatures in the 290–330 °C range, but samples collected about 380 m higher, from the 889 m level, had equilibration temperatures around 190–220 °C. This indicates that temperature decreased gradually while the ore-forming fluid migrated upwards. Karup-Møller (1977) suggested that most sulphosalt minerals in the Ag–Cu–Pb–Bi–S system are formed between 200 °C and 400 °C. These mineral temperatures are consistent with the homogenization temperatures determined for the DMJS deposit.

Currently, the available data indicate that wolframite is formed from weak acidic solutions (with pH 4.6–7.6) but scheelite is formed in alkaline aqueous conditions (with pH > 8). Zhao et al. (1977) showed that the contents of FeO and MnO in wolframite were controlled neither by experimental temperature nor by the activity of Fe^{2+} or Mn^{2+} in the ore-forming fluid but their abundances were closely related to the pH of the ore-forming fluid. The FeO/MnO ratios in wolframite ranged from around 7 to 22 when pH was between 9 and 13; the ratio approached two, at pH 8 but was less than two at pH 7. The FeO/MnO ratio in the wolframite from the DMJS deposit was 1.5–2.0 (Table 4), indicating that the DMJS ore-forming fluid was alkaline (with pH 7–8), weak alkaline conditions. As the ore-forming fluid evolved from acid to alkaline conditions, pH favored a shift from wolframite to scheelite formation.

5.2.2. Oxygen fugacity

The isotopic composition of sulfur in hydrothermal minerals is strongly controlled by the f_{O2} and pH of the hydrothermal fluids as well as by temperature and the isotopic composition of sulfur in the fluids (Ohmoto, 1972). This theory is widely used to estimate oxygen fugacity using the values of pH, temperature, and $\delta^{34}S$ (from the coexisting sulfide minerals of galena, pyrite and sphalerite at the DMJS deposit). From the pH, temperature and $\delta^{34}S$ at the DMJS deposit (see Section 5.2.1 and Table 5), we concluded that the oxygen fugacity ($\log f_{O2}$) of the ore-forming hydrothermal fluid was between −37.5 and −38.5, when the temperature was 250 °C (Fig. 7, Table 5). We observed that the variations in pyrite oxygen fugacity values were significantly larger than those in galena and sphalerite (Fig. 7). This is consistent with their paragenesis; precipitation of pyrite occurs through all four stages of mineral formation, whereas the formation of galena and sphalerite is limited to the sulfur stage. Because temperature and oxygen fugacity are positively correlated, oxygen fugacity decreased on cooling. Hence, the values of −37.5 to −38.5 were likely the $\log f_{O2}$ of the main metallogenic stage. The actual range of $\log f_{O2}$ was clearly larger, reflecting temperatures and other geological factors.

In an experimental study of the ore-forming conditions for a cassiterite–sulfide deposit in Dachang, China, the main factors affecting the mineral assemblage were determined to be temperature, oxygen fugacity, and the relative ratio of metal ion concentrations in solution (Cook and Ciobanu, 2002; Yang, 1985). The types and concentrations of the metal ions, pH, and pressure had less effect on the mineral assemblage. The elements Sn, Fe, Zn, and Cu mainly form sulfides when $\log f_{O2}$ is low ($\log f_{O2} \le -40$). Tin oxides and sulfides were formed when the oxygen fugacity was between −40 and −28. The $\log f_{O2}$ values for the DMJS tungsten polymetallic deposit suggest that wolframite, scheelite, and cassiterite formed under high oxygen fugacity conditions whereas intergrowths of pyrite, chalcopyrite, and arsenopyrite formed under a lower oxygen fugacity as temperature cooled from 330 °C to 190 °C. This is consistent with our microscopy observations of large amounts of Cu–As–Pb–Zn sulfides intergrown with wolframite, scheelite, and cassiterite.

Table 4
Chemical compositions of wolframite and scheelite in the DMJS deposit (mol.%).

Number	Mineral	FeO	MnO	CaO	WO_3
588-32-5	Wolframite	43.43	21.27	–	35.40
628-6-1	Wolframite	39.49	26.89	–	33.62
628-6-2	Wolframite	39.52	26.82	–	33.66
726-5-1	Wolframite	44.67	21.25	–	34.08
726-5-1	Scheelite	–	–	65.72	34.28
588-32-5	Scheelite	–	–	64.34	35.66

Table 5
Sulfur isotopic compositions of pyrite, galena and sphalerite.

Mineral	$\delta^{34}S$	Mineral	$\delta^{34}S$	Mineral	$\delta^{34}S$
Pyrite	−4.93	Pyrite	−0.2	Galena	−2.92
Pyrite	−4.77	Pyrite	−0.64	Galena	−3.03
Pyrite	−3.84	Pyrite	−0.44	Galena	−3.07
Pyrite	−2.52	Pyrite	−0.35	Sphalerite	−3.52
Pyrite	−1.08	Pyrite	−0.3	Sphalerite	−2.13
Pyrite	−1.05	Pyrite	−0.06	Sphalerite	−2.03
Pyrite	−0.79	Galena	−3.82	Sphalerite	−1.52

5.2.3. Sulfur fugacity

Using paragenetic information from the sulfide assemblages (pyrite, chalcopyrite, arsenopyrite, pyrrhotite, galena, marmatite, etc.) and mineral assemblage balance calculations, we can construct a record of sulfur fugacity ($\log f_{S2}$) with respect to temperature ($\log f_{S2}$-T plot; Fig. 8b) (Afifi et al., 1988a, 1988b; Simon and Essene, 1996; Zhu and Liu, 1990). As we have obtained the sulfide assemblages (galena, sphalerite, pyrite, native bismuth, bismuthinite, etc., Fig. 3), related theories and diagrams from previously published work (Afifi et al., 1988a, 1988b; Simon and Essene, 1996; Zhu and Liu, 1990; Fig. 8), and temperature (fluid inclusion test), we estimate that the $\log f_{S2}$ values for the DMJS deposit ranged from −9.7 to −37 (Fig. 8b). These values are consistent with the mineral assemblages and the proposed paragenetic sequence for the DMJS deposit. Chalcopyrite and arsenopyrite formed first, growing throughout the whole sulfur stage. Galena and sphalerite formed later and bismuth minerals formed last during the middle to late sulfur stage. Pyrite was formed during all stages.

Arsenopyrite, one of the earliest sulfides formed, is common in the DMJS deposit. Its As and S contents are sensitive to changes in temperature and $\log f_{S2}$ (Clark, 1960; Kretschmar and Scott, I976; Sharp et al., 1985). We determined the content of As in the arsenopyrite from EPMA to be 42.45–49.96 wt.% (or 30.55–35.85 at.%). Combining the

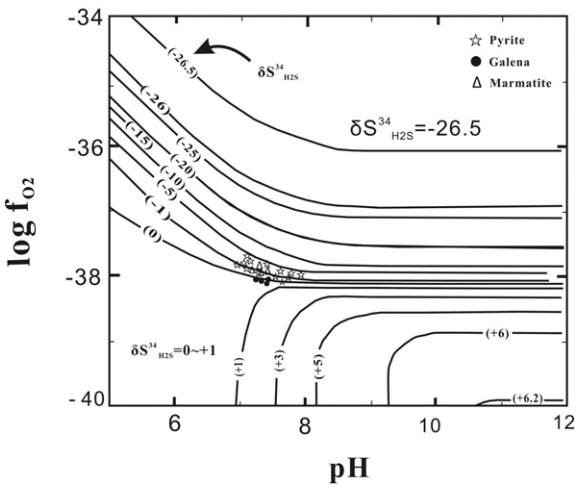

Fig. 7. Oxygen fugacity ($\log f_{O2}$) (T = 250 °C) in the DMJS deposit (modified after Ohmoto, 1972). Value of $\log f_{O2}$ is estimated by the pH, temperature, $\delta^{34}S$, the diagram and theory of Ohmoto (1972). And we have obtained the data of pH, temperature and $\delta^{34}S$ of DMJS deposit through the analysis of EPMA, fluid inclusion and sulfur isotope.

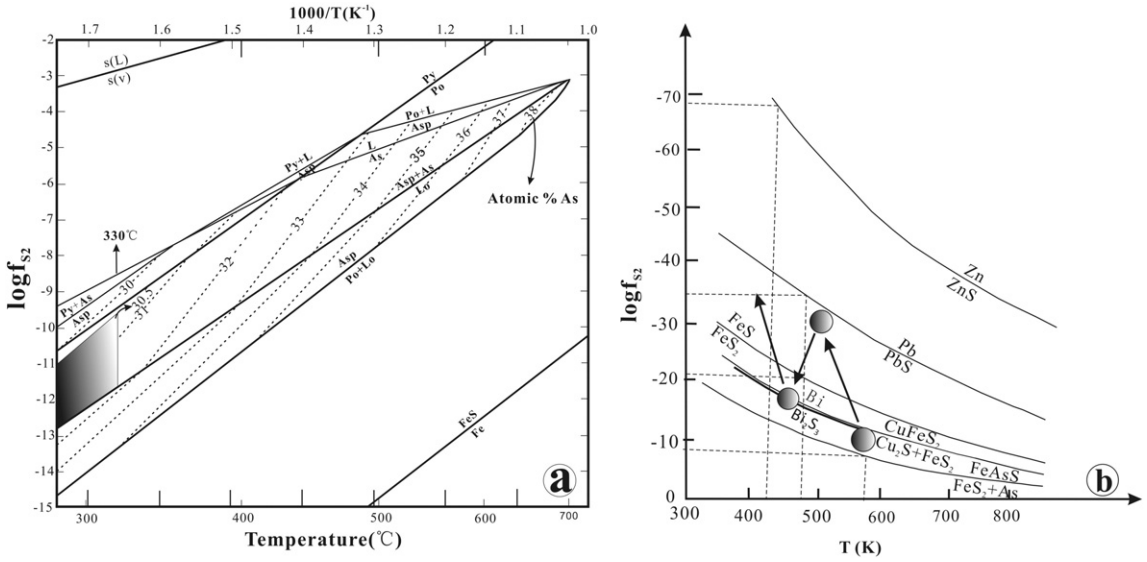

Fig. 8. (a) Relationship between arsenopyrite composition (atom per cent of As), temperature, and sulfur fugacity (logf$_{S2}$) (modified after Liu and Li, 1991; Ulrich, Kretschmar and Scott, 1976). The As and S contents of arsenopyrite are sensitive to changes in temperature and logf$_{S2}$ (Clark, 1960; Kretschmar and Scott, I976; Sharp et al., 1985). We determine the content of As in arsenopyrite from EPMA to be 42.45–49.96 wt.% (or 30.55–35.85 at.%). Combining the above data and the homogenization temperature of fluid inclusions, we estimate that the logf$_{S2}$ was −9.7 to −12.7 for the temperature range 280–330 °C (Fig. 8a) (Liu and Li, 1991; Kretschmar and Scott, 1976). (b) The logf$_{S2}$-T diagram for paragenetic sulfide assemblages (Afifi et al., 1988a, 1988b; Simon and Essene, 1996; Zhu and Liu, 1990). Using paragenetic information from the sulfide assemblages and mineral assemblages balance calculations, we can obtain a record of sulfur fugacity (logf$_{S2}$) with respect to temperature (logf$_{S2}$-T). As we have obtained the sulfide assemblages (galena, sphalerite, pyrite, native bismuth, bismuthinite, etc., Fig. 3), related theories and diagrams from previously published work (Afifi et al., 1988a, 1988b; Simon and Essene, 1996; Zhu and Liu, 1990; Fig. 8) and temperature (fluid inclusion analysis), we estimate that the values for logf$_{S2}$ of DMJS deposit ranges from −9.7 to −37.

above data and the homogenization temperatures from the fluid inclusions, we calculated that the logf$_{S2}$ was −9.7 to −12.7 for the temperature range 280–330 °C during the formation of arsenopyrite (Fig. 8a) (Liu and Li, 1991; Kretschmar and Scott, 1976), which is higher than other sulfides. This is consistent with geological observation that arsenopyrite formed first and grew throughout the whole sulfur stage at the DMJS deposit. The broad atomic ratio of As in the arsenopyrite also indicates that arsenopyrite can be formed in a wide range of sulfur fugacities.

5.3. Implication on hydrothermal evolution and ore genesis

Bismuth-antimony activation is related to moderate–high temperature hydrothermal activity (Qiu et al., 2009; Ye et al., 2014), therefore bismuth- and antimony-bearing minerals are commonly enriched in post-magmatic hydrothermal fluids. They are restricted by sulfur fugacity, oxygen fugacity, and pH as well as by the concentrations of Pb^{2+}, Bi^{3+}, and Sb^{3+} in the ore-forming fluids. The occurrence of Pb–Bi- and Pb–Sb-sulphosalts is clearly related to its special geologic context, magmatic and mineralization events (Ciobanu et al., 2010).

In the quartz–sulfide stage, a large amount of chalcopyrite and arsenopyrite were formed in the DMJS deposit. Later, scheelite and some wolframite, molybdenite, and cassiterite were formed in the early sulfide–oxide stage. We infer from this that the hydrothermal fluids had high logf$_{S2}$ and low logf$_{O2}$ in the quartz–sulfide stage. With sulfur being consumed by the precipitation of the sulfide minerals and a large quantity of H_2O and CO_2 derived from the country rocks and xenoliths, entering the magma and releasing oxygen, the hydrothermal fluid

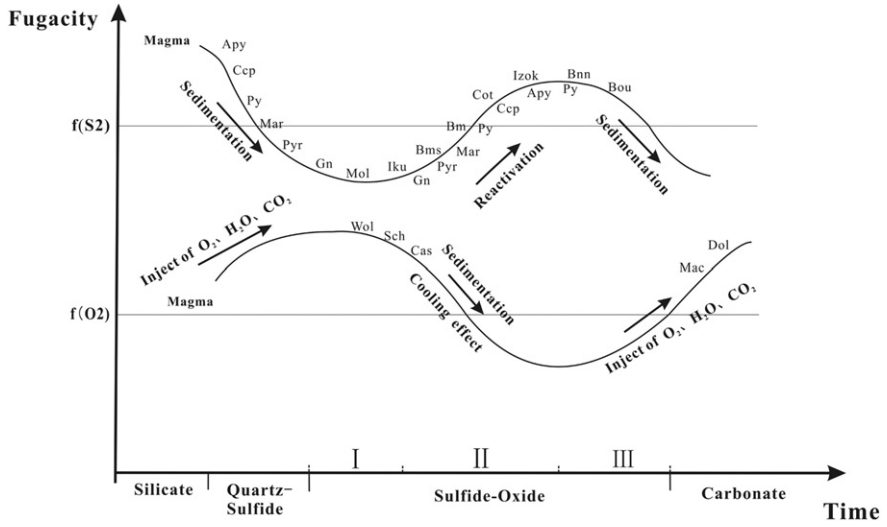

Fig. 9. The relationship between sulfur fugacity (logf$_{S2}$), oxygen fugacity (logf$_{O2}$), and the mineral evolution sequence over time. Apy—arsenopyrite, Ccp—chalcopyrite, Py—pyrite, Mar—marmatite, Pyr—pyrrhotite, Gn—galena, Mol—molybdenite, Iku—ikunolite, Bsm—native bismuth, Bm—bismuthinite, Cot—cosalite, Izok—izoklakeite, Bou—boulangerite, Bnn—bournonite, Wol—wolframite, Sch—scheelite, Cas—cassiterite, Mac—manganocalcite, Dol—dolomite.

became a high $logf_{O2}$–low $logf_{S2}$ fluid during the early part of the sulfide–oxide stage (stage (I)). Bismuth migrates in the form of $Bi_2S_2(OH)_2^0$ and $HBi_2S_4^-$ in the early stages of high temperature hydrothermal evolution, and the production of Bi-melts from hydrothermal fluids in nature can result from a number of fluid–rock or fluid–fluid reactions (Tooth et al., 2011). The $Bi_2S_2(OH)_2^0$ and $HBi_2S_4^-$ occurred desulphurization and began to decompose into native bismuth under the condition of the sulfur fugacity decrease which was lead by the decrease of the fluid temperature and the precipitation consuming large amounts of sulfur in the early stage (Ciobanu et al., 2005, 2006; Skirrow and Walshe, 2002; Tooth et al., 2008, 2011; Zaw et al., 1999). In many cases the Bi minerals occur as droplets or droplet-derived patches hosted within common ore minerals (Ciobanu and Cook, 2002; Ciobanu et al., 2005). Such morphologies are highly indicative of precipitation in a molten state. These morphologies support that their origin as polymetallic melts formed during metamorphism of a pre-existing ore (Tomkins and Mavrogenes, 2002). There was no precipitation of native bismuth in the silicate, quartz–sulfide, or the early quartz–oxide stages (I) because those sulfur-rich stages had temperatures higher than the melting point of native bismuth and the bismuth occurred as $Bi_2S_2(OH)_2^0$ and $HBi_2S_4^-$.

In the middle of the sulfide–oxide stage (II), the dissolution of As minerals is likely to result in locally highly reducing conditions (Pokrovski et al., 2002), along with the desulfurization of the bismuth complex and the reactivation of sulfides formed in the early stages. The $logf_{S2}$ of the ore-forming fluid increased leading to the formation of bismuth–antimony sulfosalt minerals under sulfur-rich conditions. Meanwhile, $Bi_2S_2(OH)_2^0$ and $HBi_2S_4^-$ decomposed into native bismuth. Above 271 °C, bismuth was molten, but milk-drop or irregular granular textures developed along the surfaces, boundaries, fractures, and vugs within galena, sphalerite, bismuthinite, and chalcopyrite, as temperature dropped. Surfaces of native bismuth always have dissolution pits (Zheng et al., 2009). The removal of large amounts of W consumed the oxygen, decreasing $logf_{O2}$ in the ore-forming fluid. Thus, the hydrothermal fluid gradually evolved to a high $logf_{S2}$–low $logf_{O2}$ fluid.

In the later sulfide–oxide (III) and carbonate stages, the metallogenic hydrothermal fluid again evolved to high $logf_{O2}$–low $logf_{S2}$, as it moved towards the surface (Fig. 9). In such a dynamic hydrothermal environment, different batches of fluid experienced different degrees of fluid–rock interaction (Brugger et al., 2000, 2008; Sung et al., 2009), and episodes of rapid mineral growth can be followed by some dissolution (Ciobanu et al., 2005; Tooth et al., 2011). These changing conditions are what produced a great number of different minerals in the DMJS deposit (including Pb–Bi- and Pb–Sb-sulphosalts) and complex compositions.

6. Conclusions

In this study, detailed mineralogical observations have been conducted to confirm mineral assemblage and the relationships between minerals in the DMJS tungsten polymetallic deposit. A large number of Pb–Bi- and Pb–Sb-sulphosalts (like izoklakeite, bournonite, cosalite, and boulangerite) were found in this deposit, providing the data to decipher the process of mineralization. Using paragenetic mineral assemblages, fluid inclusion temperatures, EPMA data, and sulfur isotopic compositions, the physicochemical conditions under which the ore formed were estimated. Results indicated that the sulfur fugacity ($logf_{S2}$) ranged from −9.7 to −37 with ore-forming temperatures in the range 190–330 °C; the oxygen fugacity ($logf_{O2}$) ranged from −37.5 to −38.5 at a model temperature of 250 °C, conditions favorable for the formation of a tungsten polymetallic deposit. Variations of the physicochemical conditions could be responsible for specific mineral assemblage. Our mineralogical studies provide new information on tungsten mineralization and further exploration of tungsten resources in the Sanjiang Tethyan mineral belt.

Conflict of interest

The authors declare that they have no conflicts of interest to this work and there are no known conflicts of interest associated with this publication.

Acknowledgments

The authors acknowledge Guofu Zhou, Shaohua Dong and Lin Ye for their help with EPMA analyses and explanation. We also thank sincerely Prof. Cristiana L. Ciobanu for her constructive comments to help greatly improve this manuscript. This work was financially supported by 973 Program (2014CB440904), National Natural Science Foundation of China (Grant Nos. 40930425, 41173026), CAS/SAFEA International Partnership Program for Creative Research Teams (KZZD-EW-TZ-20), and The 12th Five-Year Plan project of State Key Laboratory of Ore-deposit Geochemistry, Chinese Academy of Sciences (SKLODG-ZY125-07).

References

Achimovičová, M., Balaž, P., 2008. Kinetics of the leaching of mechanically activated berthierite, boulangerite and franckeite. Phys. Chem. Miner. 35 (2), 95–101.
Afifi, A.M., Kelly, W.C., Essene, E.J., 1988a. Phase relations among tellurides, sulfides, and oxides; I, Thermochemical data and calculated equilibria. Econ. Geol. 83 (2), 377–394.
Afifi, A.M., Kelly, W.C., Essene, E.J., 1988b. Phase relations among tellurides, sulfides, and oxides; Pt. II, Applications to telluride-bearing ore deposits. Econ. Geol. 83 (2), 395–404.
Brugger, J., Lahaye, Y., Costa, S., Lambert, D., Bateman, R., 2000. Inhomogenous distribution of REE in scheelite and dynamics of Archaean hydrothermal systems (Mt Charlotte and Drysdale gold deposits, Western Australia). Contrib. Mineral. Petrol. 139, 251–264.
Brugger, J., Etschmann, B., Pownceby, M., Liu, W.H., Grundler, P.V., Brewe, D., 2008. Oxidation state of europium in scheelite: tracking fluid–rock interaction in gold deposits. Chem. Geol. 257, 26–33.
Chatterjee, A.K., Smith, P.K., 2000. Co-existing electrum, bismuth, galena and plumbean sulfotellurides. Beaver Dam Gold Deposit: Implication for thermometry of hydrothermal veins. In: Mining Matters for Nova Scotia 2000 – Opportunities for Economic Development, Abstracts.
Ciobanu, C.L., Cook, N.J., 2002. Tellurides, selenides (and Bi-sulphosalts) in gold deposits. 11th IAGOD Symp-Geocongress, CD vol, GeolSurv Namibia.
Ciobanu, C.L., Cook, N.J., Pring, A., 2005. Bismuth tellurides as gold scavengers. In: Mao, J.W., Bierlein, F.P. (Eds.), Mineral Deposit Research: Meeting the Global Challenge. Springer, Berlin-Heidelberg-New York, pp. 1383–1386.
Ciobanu, C.L., Cook, N.J., Damian, F., Damian, G., 2006. Gold scavenged by bismuth melts: An example from Alpine shear-remobilizates in the Highiş Massif, Romania. Mineral. Petrol. 87 (3–4), 351–384.
Ciobanu, C.L., Birch, W.D., Cook, N.J., Pring, A., Grundler, P.V., 2010. Petrogenetic significance of Au–Bi–Te–S associations: the example of Maldon, Central Victorian gold province, Australia. Lithos 116 (1), 1–17.
Clark, L.A., 1960. The Fe–As–S system–Phase relations and applications. Econ. Geol. 55 (7), 1345–1381.
Cook, N., Ciobanu, C., 2002. Tellurides: More than mineralogical curiosities, but also markers of fS2–fO2 evolution in zoned hydrothermal systems. IMA, 18th General Meeting, Edinburgh, p. 283.
Cook, N.J., Ciobanu, C.L., Howard, W.R., 2007a. Bi-tellurides in gold veins BiTeI Knoll (CLY prospect) southeastern British Columbia, Canada.
Cook, N.J., Ciobanu, C.L., Stanley, C.J., Paar, W.H., Sundblad, K., 2007b. Compositional data for Bi–Pb tellurosulfides. Can. Mineral. 45 (3), 417–435.
Cook, N.J., Ciobanu, C.L., Williams, T., 2011. The mineralogy and mineral chemistry of indium in sulphide deposits and implications for mineral processing. Hydrometallurgy 108 (3), 226–228.
Deng, J., Hou, Z.Q., Mo, X.X., Yang, L.Q., Wang, Q.F., Wang, C.M., 2010. Superimposed orogenesis and metallogenesis in Sanjiang Tethys. Miner. Depos. 29 (01), 37–42 (in Chinese with English abstract).
Deng, J., Wang, C.M., Li, G.J., 2012. Style and process of the superimposed mineralization in the Sanjiang Tethys. Acta Petrol. Sin. 28 (5), 1349–1361 (in Chinese with English abstract).
Deng, J., Yang, L.Q., Wang, C.M., 2011. Research advances of superimposed orogenesis and metallogenesis in the Sanjiang Tethys. Acta Petrological Sinica 27 (9), 2501–2509 (in Chinese with English abstract).
Deng, J., Wang, Q.F., Li, G.J., Li, C.S., Wang, C.M., 2014a. Tethys tectonic evolution and its bearing on the distribution of important mineral deposits in the Sanjiang region, SW China. Gondwana Res.
Deng, J., Wang, C.M., Li, W.C., Wang, Q.F., 2014b. The situation and enlightenment of the research of the tectonic evolution and metallogenesis in the Sanjiang Tethys. Earth Sci. Front. 21 (01), 52–64 (in Chinese with English abstract).
Dimitrova, D., Kerestedjian, T., 2006. Bismuth minerals in the postskarn sulphide–arsenide mineralization in the Martinovo iron deposit, NW Bulgaria. Geochem. Mineral. Petrol. (Sofia) 44, 19–32.

Harris, D., Roberts, A., 1986. Izoklakeite, A new mineral species from Izok Lake, Northwest Territories. Can. Mineral. 24, 1–5.
Hou, Z.Q., Wang, L., Zaw, K., 2003. Post-collisional crustal extension setting and VHMS mineralization in the Jinshajiang orogenic belt, southwestern China. Ore Geology Reviews 22, 177–199.
Hou, Z.Q., Zaw, K., Pan, G.T., Mo, X.X., Xu, Q., Hu, Y.Z., Li, X.Z., 2007a. Sanjiang Tethyan metallogenesis in SW China: Tectonic setting, metallogenic epochs and deposit types. Ore Geol. Rev. 31 (1), 48–87.
Hou, Z.Q., Pan, X.F., Yang, Z.M., Qu, X.M., 2007b. Porphyry Cu-(Mo–Au) deposits no related to oceanic-slab subduction examples from Chinese porphyry deposits in continental settings. Geoscience 21 (02), 332–351 (in Chinese with English abstract).
Hu, R.Z., Burnard, P., Bi, X.W., Zhou, M.F., Pen, J.T., Su, W.C., Wu, K.X., 2004. Helium and argon isotope geochemistry of alkaline intrusion-associated gold and copper deposits along the Red River—Jinshajiang fault belt, SW China. Chem. Geol. 203 (3), 305–317.
Jin, B.H., 1986. Reference samples for electron probe microanalysis. Rock Miner. Anal. 5 (2), 157–163 (in Chinese with English abstract).
Karup-Møller, S., 1977. Mineralogy of some Ag–(Cu)–Pb–Bi sulphide associations. Bull. Geol. Soc. Denmark 26, 41–68.
Kostov, I., Stefanova, J.M., 1981. Sulphide Minerals. Crystal Chemistry, Parageneses and Systematics. Bulgarian Academy of Sciences. Institute of Geology (212 págs).
Koszowska, E., 2004. Preliminary report on tellurium and bismuth mineralization in skarn from Zawiercie, Southern Poland. Mineral. Soc. of Poland, Special papers 24, 231–234.
Kretschmar, U., Scott, S., 1976. Phase relations involving arsenopyrite in the system Fe-As-S and their application. Canadian Mineralogist 14 (3), 364–386.
Li, X.Z., Liu, W.J., Wang, Y.Z., 1999. Tethys tectonic evolution and mineralization in the Sanjiang area (pandect). Geological Publishing House, Beijing, pp. 1–276 (in Chinese).
Liu, Y.F., Li, C.Y., 1991. Study of physical and chemical condition controlling ore formation of the gold, silver, base-metal ore deposit of pyrite-type in Donggouba, Lueyang, Shanxi. Mineral. Petrol. 11 (2), 155–164 (in Chinese with English abstract).
Liu, Z.Q., Li, X.Z., Ye, Q.T., 1993. Division of tectono-magmatic zone and distribution of mineral in the Sanjiang Region [M]. Geol. Pub. House, Beijing, p. 246 (in Chinese).
Luo, S.H., Jiang, S.Z., 1992. Sulfosalt minerals and the distribution characteristics in Hunan. China Academic Journal Electronic Publishing House, China (in Chinese with English abstract).
Martínez Frías, J., 1991. Sulphide and sulphosalt mineralogy and paragenesis from the Sierra Almagrera veins, Betic Cordillera (SE Spain). Estud. Geol. 47 (5–6), 271–279.
Ohmoto, H., 1972. Systematics of sulfur and carbon isotopes in hydrothermal ore deposits. Econ. Geol. 67 (5), 551–578.
Pan, G.T., Chen, Z.L., Li, X.Z., 1997. The tectonic evolution of eastern Tethys. Geological Publishing House, Beijing, pp. 28–101 (in Chinese).
Pan, G.T., Wang, L.Q., Yin, F.G., Zhu, D.C., Geng, Q.R., Liao, Z.L., 2004. Charming of landing of plate tectonics on the continent as viewed from the study of the archipelagic arc-basin system. Geological Bulletin of China 23 (9-10), 933–939 (in Chinese with English abstract).
Pokrovski, G.S., Kara, S., Roux, J., 2002. Stability and solubility of arsenopyrite, FeAsS, in crustal fluids. Geochim. Cosmochim. Acta 66, 2361–2378.
Pruseth, K.L., Mishra, B., Bernhardt, H.-J., 2001. The minerals boulangerite, falkmanite and Cu-free meneghinite: synthesis, new powder diffraction data and stability relations. Eur. J. Mineral. 13 (2), 411–419.
Qiu, S.D., Wang, B.H., Xu, J.H., Xie, Y.L., 2009. Ingodite found for the first time in China. Acta Mineral. Sin. 28 (4), 357–359 (in Chinese with English abstract).
Ramdohr, P., 1980. The Ore Minerals and Their Intergrowths. Oxford, Pergamon Press 109–127, 436–437.
Sharp, Z.D., Essene, E.J., Kelly, W.C., 1985. Are-examination of the arsenopyrite geothermometer: pressure considerations and applications to natural assemblages. J. Mineral. Assoc. Can. 23 (Part 4).
Simon, G., Essene, E.J., 1996. Phase relations among selenides, sulfides, tellurides, and oxides; I, Thermodynamic properties and calculated equilibria. Econ. Geol. 91 (7), 1183–1208.
Skirrow, R.G., Walshe, J.L., 2002. Reduced and oxidized Au–Cu–Bi iron oxide deposits of the Tennant Creek Inlier, Australia: An integrated geologic and chemical model. Econ. Geol. 97 (6), 1167–1202.
Sone, M., Metcalfe, I., 2008. Parallel Tethyan sutures in mainland Southeast Asia: new insights for Palaeo-Tethys closure and implications for the Indosinian orogeny. C. R. Geosci. 340 (2), 166–179.
Sun, X., Zhang, Y., Xiong, D., Sun, W., Shi, G., Zhai, W., Wang, S., 2009. Crust and mantle contributions to gold-forming process at the Daping deposit, Ailaoshan gold belt, Yunnan, China. Ore Geol. Rev. 36 (1), 235–249.
Sung, Y.H., Brugger, J., Ciobanu, C.L., Pring, A., Skinner, W., Nugus, M., 2009. Invisible gold in arsenian pyrite and arsenopyrite from a multistage Arcaean gold deposit: Sunrise Dam, Eastern Goldfields Province, Western Australia. Mineral. Deposita 44, 765–791.
Tomkins, A.G., Mavrogenes, J.A., 2002. Mobilization of gold as a polymetallic melt during pelite anatexis at the Challenger deposit, South Australia: a metamorphosed Archean gold deposit. Econ. Geol. 97 (6), 1249–1271.
Tooth, B., Brugger, J., Ciobanu, C.L., Liu, W., 2008. Modeling of gold scavenging by bismuth melts coexisting with hydrothermal fluids. Geology 36 (10), 815–818.
Tooth, B., Ciobanu, C.L., Green, L., O'Neill, B., Brugger, J., 2011. Bi-melt formation and gold scavenging from hydrothermal fluids: An experimental study. Geochim. Cosmochim. Acta 75 (19), 5423–5443.
Ventruti, G., Stasi, F., Pinto, D., Vurro, F., Renna, M., 2012. The plumose boulangerite from bottino, Apuan Alps, Italy: crystal structure, OD character and twinning. Can. Mineral. 50 (2), 181–199.
Wagner, T., Jonsson, E., 2001. Mineralogy of sulfosalt-rich vein-type ores, Boliden massive sulfide deposit, Skellefte district, northern Sweden. Can. Mineral. 39 (3), 855–872.
Wagner, T., Jonsson, E., Boyce, A.J., 2005. Metamorphic ore remobilization in the Hällefors district, Bergslagen, Sweden: constraints from mineralogical and small-scale sulphur isotope studies. Mineral. Deposita 40 (1), 100–114.
Wang, W.K., Niu, X.X., 1994. Study on morphology of some sulfide minerals. Earth Sci. J. China Univ. Geosci. 19 (2), 157–168 (in Chinese with English abstract).
Wang, C.M., Deng, J., Zhang S.T., , Xue, C.J., Yang, L.Q., Wang, Q.F., Sun, X., 2010a. Sediment-hosted Pb-Zn deposits in southwest Sanjiang Tethys and Kangdian area on the western margin of Yangtze Craton. Acta Geologica Sinica 84 (6), 1428–1438.
Wang, C.M., Deng, J., Zhang, S.T., Yang, L.Q., 2010b. Metallogenic province and large scale mineralization of VMS deposits in China. Resource Geology 60, 404–413.
Wang, C.M., Deng, J., Carranza, E.J.M., Santosh, M., 2014. Tin metallogenesis associated with granitoids in the southwestern Sanjiang Tethyan Domain: nature, deposit types, and tectonic setting. Gondwana Research 26 (2), 576–593.
Wei, P.J., Zhang, H.J., 1991. The first-time discovery of izoklakeite in China. Geoscience 5 (2), 184–191 (in Chinese with English abstract).
Xu, G.F., Shao, J.L., 1982. The problem of determining Pb–Sb sulphosal is hardly yielding to identification. Mineral. Petrol. 4 (2), 26–50 (in Chinese with English abstract).
Xue, C., Zeng, R., Liu, S., Chi, G., Qing, H., Chen, Y., Yang, J., Wang, D., 2007. Geologic, fluid inclusion and isotopic characteristics of the Jinding Zn–Pb deposit, western Yunnan, South China: a review. Ore Geol. Rev. 31 (1), 337–359.
Yang, J.S., 1985. An experimental study of the ore-forming conditions of a cassiterite–sulphide deposit in Dachang, China. Miner. Resour. Geol. 3 (7), 53–58 (in Chinese with English abstract).
Ye, L., Liu, T., Yang, Y., Gao, W., Pan, Z., Bao, T., 2014. Petrogenesis of bismuth minerals in the Dabaoshan Pb–Zn polymetallic massive sulfide deposit, northern Guangdong Province, China. J. Asian Earth Sci. 82, 1–9.
Yin, G.F., Pan, G.T., Wang, F., Li, X.Z., Wang, F.G., 2006. Tectonic facies along the Nujiang–Lancangjiang–Jinshajing orogenic belt in southwestern China. Sediment. Geol. Tethyan Geol. 26 (4), 33–39 (in Chinese with English abstract).
Zakrzewski, M.A., Makovicky, E., 1986. Izoklakeite from Vena, Sweden, and the kobellite homologous series. Can. Mineral. 24, 7–18.
Zaw, K., 1990. Geological, petrogical and geochemical characteristics of granitoid rocks in Burma: with special reference to the associated W–Sn mineralization and their tectonic setting. J. SE Asian Earth Sci. 4 (4), 293–335.
Zaw, K., Huston, D., Large, R., 1999. A chemical model for the Devonian remobilization process in the Cambrian volcanic-hosted massive sulfide Rosebery deposit, western Tasmania. Econ. Geol. 94 (4), 529–546.
Zhang, C.H., 2000. The gold and rare metal deposits in the northeast of Russia. J. Precious Met. Geol. 9 (2), 123–128 (in Chinese).
Zhang, Y., Han, R.S., Wu, P., Wei, P.T., 2013. Logf_{O2}–logf_{S2} facies map of mineral assemblage model of sandstone-hosted copper deposits—Taking the Dayao Liuju copper deposit for example. J. Mineral. Petrol. 33 (2), 35–42 (in Chinese with English abstract).
Zhao, B., Li, W.X., Cai, Y.J., 1977. Conditions of formation of wolframite, cassiterite, columbite, microlite, and tapiolite, and experimental studies on the variation of Nb and Ta in wolframite and cassiterite. Geochimica 2, 125–137 (in Chinese with English abstract).
Zheng, B., An, F., Zhu, Y.F., 2009. Native bismuth found in Baogutu gold deposit and its geological significance. Acta Petrol. Sin. 25 (6), 1426–1436 (in Chinese with English abstract).
Zhong, C.H., Xu, J.H., Ding, R.F., Mao, Q., Xie, Y.L., 2005. Native bismuth in Sarekoubo gold deposit and its relation to gold mineralization. Bull. Mineral. Petrol. Geochem. 21 (2), 130–134 (in Chinese with English abstract).
Zhu, Y.N., Liu, C.Z., 1990. Geochemical studies on ore-forming process of the Hetai gold deposit. J. Guilin Coll. Geol. 10 (3), 291–298 (in Chinese with English abstract).
Zi, J.-W., Cawood, P.A., Fan, W.-M., Tohver, E., Wang, Y.-J., McCuaig, T.C., Peng, T.-P., 2013. Late Permian–Triassic magmatic evolution in the Jinshajiang orogenic belt, SW China and implications for orogenic processes following closure of the Paleo-Tethys. Am. J. Sci. 313 (2), 81–112.